PHYSICAL REVIEW E **96**, 023108 (2017)

# Influence of the temperature-dependent viscosity on convective flow in the radial force field

Vadim Travnikov,[1,*] Florian Zaussinger,[1,†] Philippe Beltrame,[2,‡] and Christoph Egbers[1,§]
[1]*Department of Aerodynamics and Fluid Mechanics, Brandenburg University of Technology Cottbus-Senftenberg, Siemens-Halske-Ring 14, D-03046, Cottbus, Germany*
[2]*UMR1114, Université d'Avignon–INRA, F-84000 Avignon, France*

(Received 21 March 2017; published 29 August 2017)

The numerical investigation of convective flows in the radial force field caused by an oscillating electric field between spherical surfaces has been performed. A temperature difference ($T_1 > T_2$) as well as a radial force field triggers a fluid flow similar to the Rayleigh-Bénard convection. The onset of convective flow has been studied by means of the linear stability analysis as a function of the radius ratio $\eta = R_1/R_2$. The influence of the temperature-dependent viscosity has been investigated in detail. We found that a varying viscosity contrast $\beta = \nu(T_2)/\nu(T_1)$ between $\beta = 1$ (constant viscosity) and $\beta = 50$ decreases the critical Rayleigh number by a factor of 6. Additionally, we perform a bifurcation analysis based on numerical simulations which have been calculated using a modified pseudospectral code. Numerical results have been compared with the GeoFlow experiment which is located on the International Space Station (ISS). Nonturbulent three-dimensional structures are found in the numerically predicted parameter regime. Furthermore, we observed multiple stable solutions in both experiments and numerical simulations, respectively.

DOI: 10.1103/PhysRevE.96.023108

## I. INTRODUCTION

Buoyancy driven convective flows play a crucial role in geophysical and astrophysical research, and furthermore in the understanding of dynamos in the core of planets. Radial fields induced by means of an artificial electric force field in the spherical gap and coupled with temperature can be used to investigate convective flows in geophysics and astrophysics numerically and experimentally as well. Furthermore, a mechanism of the artificial gravity is useful for the flow control and heat transfer. To trigger such flows the influence of the Earth's gravity must be eliminated and heating source has to be placed to enable the artificial buoyancy force. The first condition can be satisfied by performing the experiment under microgravity conditions, e.g., on the International Space Station (ISS). A possibility to realize the second one is to set a temperature difference between surfaces, say the inner surface is warmer than the outer one ($T_1 > T_2$). The radial force field is created by an electric field $\mathbf{E}$ which induces three forces. The force density generated by $\mathbf{E}$ imposed on a dielectric fluid is obtained by [1]

$$\mathbf{f}_e = \rho_e \mathbf{E} - \frac{1}{2}\mathbf{E}^2 \nabla \epsilon(T) + \nabla\left[\frac{1}{2}\rho\left(\frac{\partial \epsilon}{\partial \rho}\right)_T \mathbf{E}^2\right], \tag{1}$$

where the first term is the Coulomb force with free charge $\rho_e$. This force can be neglected as the inherent frequency is several magnitudes higher than characteristic process frequencies found in convective flows. The third one, namely electrostrictive force, is combined with the pressure gradient in the Navier-Stokes equation. The remaining second term corresponds to the dielectrophoretic force $\mathbf{f}_{\text{dep}}$. In principle, the electric permittivity $\epsilon$ is a tensor of rank 2, depending on temperature and frequency. In the case of small temperature fluctuations the electric permittivity is approximated by a linear function

$$\epsilon(T) = \epsilon_0 \epsilon_r [1 - \gamma(T - T_2)]. \tag{2}$$

The force $\mathbf{f}_{\text{dep}}$ can be written after small algebra as follows:

$$\mathbf{f}_{\text{dep}} = -\gamma(T - T_2)\mathbf{g}_e, \quad \mathbf{g}_e = \frac{\epsilon_0 \epsilon_r}{2\rho} \nabla E^2, \tag{3}$$

where $\mathbf{g}_e$ is the electric field due to the induced artificial gravity field and $\gamma$ is the thermal coefficient of the permittivity. The electric field can be found by solving the Gauss equation [2]. An expression for the gravity is simplified for large frequency $\omega$ of the applied electric field approximation: $\omega \gg \tau_e^{-1} = \sigma/\epsilon$, with electrical conductivity $\sigma$. A period averaged relation for the gravity reads

$$\mathbf{g}_e = -2V_{\text{rms}}^2 \frac{\epsilon_0 \epsilon_r}{\rho} \frac{R_1^2 R_2^2}{(R_2 - R_1)^2} \frac{1}{r^5} \mathbf{e}_r. \tag{4}$$

Because the dielectrophoretic force $\mathbf{f}_{\text{dep}}$ and the induced artificial gravity have opposite directions the problem can be compared with the classical Rayleigh-Bénard problem.

This specific problem has been considered by many authors in the case of the constant viscosity. The linear stability analysis for the radius ratios $\eta = R_1/R_2 = 0.1$–$0.7$ has been performed in [3] to investigate the onset of convection. It was found that in the nonrotating case critical Rayleigh number, obtained by means of the linear stability analysis, $\text{Ra}_{cL}$, increases with increasing in $\eta$. Moreover, the basic flow becomes unstable with respect to steady perturbations and does not depend on the Prandtl number. Perturbations have been represented in terms of spherical harmonics, $Y_\ell^m$, and because of the spherical symmetry the linear stability analysis is performed in terms of the degree $\ell$ and not of the azimuthal wave number $m$ as it occurs in rotating systems. Therefore, it is particularly important to perform nonlinear three-dimensional calculations to detect which patterns the system prefers. Busse [4] solved the pattern selection problem of the convective

---

[*] Vadim.Travnikov@b-tu.de
[†] Florian.Zaussinger@b-tu.de
[‡] Philippe.Beltrame@univ-avignon.fr
[§] Christoph.Egbers@b-tu.de

flow in the nonrotating case *analytically*, in which degree $\ell$ plays a crucial role. He found solutions with $\ell = 4$ and $\ell = 6$. Recently, the multiplicity of supercritical states has been detected in [5] by means of *numerical simulations*, using a pseudospectral code, developed by Hollerbach [6]. Octahedral and axisymmetric structures have been observed in the interval $2491 < \mathrm{Ra} < 5000$ ($\mathrm{Ra}_{cL} = 2491$), for the radius ratio $\eta = 0.5$ and Prandtl number $\mathrm{Pr} = 64.64$. Further increase in Rayleigh number up to $\mathrm{Ra} = 17450$ leads to the appearance of a seven-cell structure and periodic flow. Experimental investigations of the convective flow under the influence of the artificial gravity in the form of $\mathbf{g}_e \sim r^{-5}$ have been performed in [7] for fluids with constant viscosity like silicon oil. Spatiotemporal irregular structures have been observed for $\mathrm{Ra} = 6.0 \times 10^4$. We expect that the use of working fluids with temperature-dependent viscosity enables the occurrence of new fluid structures which can have an important geophysical application [8,9].

The microgravity experiment GeoFlow is designed to capture convective flows with these properties. This is a motivation for our numerical efforts. First experimental and numerical results [10,11] show that sheetlike flows can be observed for moderate Rayleigh numbers, and that plumelike thermal flows develop if the Rayleigh number increases. Numerical three-dimensional solutions have been obtained by using the finite-volume method. But only recently we have developed a pseudospectral numerical code which is able to perform the linear stability analysis and evaluation of three-dimensional flows as well.

Solomatov [12] characterized convection with temperature dependent viscosity as follows. Isoviscous situations and small contrasts ($\beta < 10^2$) in the viscosity belong to the mobile-lid type. Here, convective plumes reach the colder boundaries. For $10^2 < \beta < 10^4$ the sluggish-lid regime dominates the flow. The viscous boundary layer at the colder side is significantly larger than at the hotter boundaries. This reduces the velocity of convective plumes. Situations where $\beta > 10^4$ develop a stagnant lid. Convective plumes are not able to reach the cold solid boundary. Recently, Curbelo and Mancho [13,14] published results for the transient sluggish lid case. Their simulations showed traveling waves, heteroclinic connections, and chaotic regimes in a two-dimensional setup in the presence of the O(2) symmetry.

This paper is organized as follows. After discussion of governing equations in Sec. II we formulate briefly the numerical method (Sec. III) with which the problem under consideration is solved. Stability of the basic flow has been investigated by means of the linear stability theory in Sec. IV. Some examples of three-dimensional flows are presented in Sec. V A, two bifurcation scenarios and diagrams are discussed in Sec. V B, the behavior of the Nusselt number which describes the heat transfer is shown in Sec. V C, and comparison between numerical calculation and experimental results has been performed in Sec. VI.

## II. EQUATIONS

We consider an incompressible viscous dielectric fluid in the spherical gap of width $d = R_2 - R_1$. The inner surface is maintained at the warmer temperature than the outer one ($T_1 > T_2$). Introducing the following scaling $\Delta T = T_1 - T_2$ for the temperature, $\rho_0(\kappa/d)^2$ for the pressure, $d$ for the length, $\kappa/d$ for the velocity, and $t_\kappa = d^2/\kappa$ for the time, and using the Boussinesq approximation, the Navier-Stokes equation, the energy equation, and the continuity equation can be written in the dimensionless form as follows:

$$\mathrm{Pr}^{-1}\left[\frac{\partial \mathbf{U}}{\partial t} + (\mathbf{U}\cdot\nabla)\mathbf{U}\right] = -\mathrm{Pr}^{-1}\nabla P + \mathrm{Ra}\frac{\eta^2}{(1-\eta)^4}\frac{T}{r^5}\mathbf{e}_r + \nabla\cdot\left[\frac{\nu(T)}{\nu_{\mathrm{ref}}}[\nabla\mathbf{U} + (\nabla\mathbf{U})^T]\right], \tag{5}$$

$$\frac{\partial T}{\partial t} + (\mathbf{U}\cdot\nabla)T = \nabla^2 T, \tag{6}$$

$$\nabla\cdot\mathbf{U} = 0. \tag{7}$$

The flow depends on the radius ratio $\eta = R_1/R_2$, the Prandtl number $\mathrm{Pr} = \nu_{\mathrm{ref}}/\kappa = 125$ (1-Nonanol, GeoFlow II [10]), and the Rayleigh number

$$\mathrm{Ra} = \frac{2\epsilon_0\epsilon_r\gamma}{\rho\nu_{\mathrm{ref}}\kappa}V_{\mathrm{rms}}^2\Delta T,$$

where $\epsilon_r$ is the relative permittivity, $\gamma$ is the permittivity, $V_{\mathrm{rms}}^2 = V_0^2/2$ is the voltage, $\rho$ is the density, and $\nu_{\mathrm{ref}}$ is the viscosity on the outer and colder surface. The velocity should obey the no-slip boundary conditions $\mathbf{u} = 0$ and $T = 1$, $T = 0$ for the temperature on the surfaces $r = \eta/(1-\eta)$ and $r = 1/(1-\eta)$, correspondingly. The influence of the temperature-dependent viscosity is the focus of the research presented. The kinematic viscosity varies according to the Arrhenius law

$$\nu(T) = \nu_{\mathrm{ref}}e^{-(\ln\beta)T}, \tag{8}$$

where $\beta = \nu_{\mathrm{ref}}/\nu_{\mathrm{hot}} = \nu_{\mathrm{cold}}/\nu_{\mathrm{hot}}$ is the viscosity contrast that varies between $\beta = 1$ (constant viscosity) and $\beta = 50$ and must be taken into account by solving the Navier-Stokes equation. The equations (5)–(8) with the boundary conditions have to be solved numerically.

## III. NUMERICAL METHOD

The fully three-dimensional pseudospectral numerical code for the spherical geometry has been developed by Hollerbach [6] for the case of the constant viscosity. We expanded this tool on the situation when the viscosity varies according to the Arrhenius law Eq. (8). The poloidal-toroidal representation of the velocity field

$$\mathbf{U} = \nabla\times\nabla\times(\Phi\mathbf{e}_r) + \nabla\times(\Psi\mathbf{e}_r) \tag{9}$$

obeys the continuity equation. Separated equations for poloidal $\Phi$ and toroidal $\Psi$ potentials are presented in the Appendixes. After performing the mapping $r = \frac{1}{2}[z + \frac{1+\eta}{1-\eta}]$, where $z \in [-1,+1]$ each scalar function can be expanded in terms of Chebychev polynomials $T_{k-1}(z)$ in radial direction and in terms of spherical harmonics $Y_\ell^m(\theta,\phi) = P_\ell^m(\theta)e^{im\phi}$ for the angular dependence. Expressions for poloidal and toroidal potentials can be written as follows:

$$\Phi(t,r,\theta,\phi) = \sum_{m=0}^{\mathrm{MU}} \sum_{\ell=\ell'}^{\mathrm{LU}} \sum_{k=1}^{\mathrm{KU}+4} (g_{ck\ell m}(t)\cos(m\phi) + g_{sk\ell m}(t)\sin(m\phi))T_{k-1}(z)P_\ell^m(\theta), \tag{10}$$

$$\Psi(t,r,\theta,\phi) = \sum_{m=0}^{\mathrm{MU}} \sum_{\ell=\ell'}^{\mathrm{LU}} \sum_{k=1}^{\mathrm{KU}+2} (f_{ck\ell m}(t)\cos(m\phi) + f_{sk\ell m}(t)\sin(m\phi))T_{k-1}(z)P_\ell^m(\theta), \tag{11}$$

where $\ell' = \max(1,m)$, and KU, LU, and MU are cutoff parameters that vary between 20–30, 30–40, and 20–30, correspondingly. Time-dependent spectral coefficients have been calculated by means of the predictor-corrector method. The smallest time step was $\Delta t = 2 \times 10^{-5}$. Note that four boundary conditions for $\Phi$ and two for $\Psi$ are necessary (see the Appendixes).

## IV. LINEAR STABILITY ANALYSIS

The system of equations (5)–(8) has basic flow solution $\mathbf{u} = \mathbf{u}_0 = \mathbf{0}$, $T_{\mathrm{cond}} = \frac{\eta}{(1-\eta)^2}\frac{1}{r} - \frac{\eta}{1-\eta}$. In contrast to the Rayleigh-Bénard convection, the artificial gravity is not constant and depends on $r$ according to $g_e \sim r^{-5}$. Stability of the basic flow is investigated by means of linear stability theory, which is used to find such critical Rayleigh numbers, $\mathrm{Ra}_{cL}$, above which the flow becomes unstable with respect to infinitesimal perturbations.

To calculate the critical Rayleigh numbers in frames of the linear stability theory the Navier-Stokes equation as well as the energy equation have to be linearized. Furthermore, the eigenvalue problem for the radius ratios between $\eta = 0.1$–$0.7$, for different viscosity contrasts $\beta = 1$–$50$ needs to be solved, too. The basic flow is subjected to *small* perturbations $\tilde{\mathbf{u}}(t,r,\theta,\phi)$ for the velocity, $\tilde{p}(t,r,\theta,\phi)$ for the pressure, and $\Theta(t,r,\theta,\phi)$ for the temperature. Substituting the perturbed functions $\mathbf{U} = \mathbf{u}_0(=0) + \tilde{\mathbf{u}}$, $P = p_0 + \tilde{p}$, and $T = T_{\mathrm{cond}} + \Theta$ in Eqs. (5)–(8) and neglecting nonlinear terms results in

$$\mathrm{Pr}^{-1}\frac{\partial \tilde{\mathbf{u}}}{\partial t} = -\,\mathrm{Pr}^{-1}\nabla \tilde{p} + \mathrm{Ra}\frac{\eta^2}{(1-\eta)^4}\frac{\Theta}{r^5}\mathbf{e}_r + \tilde{\mathbf{f}}_0 + \frac{\nu(T_{\mathrm{cond}})}{\nu_{\mathrm{cold}}}\nabla^2\tilde{\mathbf{u}}, \tag{12}$$

$$\frac{\partial \Theta}{\partial t} - \tilde{u}_r \frac{\eta}{(1-\eta)^2}\frac{1}{r^2} = \nabla^2\Theta, \tag{13}$$

$$\nabla \cdot \tilde{\mathbf{u}} = 0, \tag{14}$$

with

$$\tilde{\mathbf{f}}_0 = \begin{pmatrix} \frac{\nu_r(T_{\mathrm{cond}})}{\nu_{\mathrm{cold}}}\tilde{D}_{rr} \\ \frac{\nu_r(T_{\mathrm{cond}})}{\nu_{\mathrm{cold}}}\tilde{D}_{r\theta} \\ \frac{\nu_r(T_{\mathrm{cond}})}{\nu_{\mathrm{cold}}}\tilde{D}_{r\phi} \end{pmatrix},$$

where $\tilde{D}_{ij}$ are components of the rate-of-strain tensor for the perturbed velocity field multiplying by 2. Equations can be formulated in terms of the poloidal-toroidal decomposition. The potential $\tilde{\Phi}$ obeys Eq. (A2) with force $\tilde{\mathbf{F}} = \mathrm{Ra}\frac{\eta^2}{(1-\eta)^4}\frac{\Theta}{r^5}\mathbf{e}_r$.

TABLE I. Critical Rayleigh numbers $\mathrm{Ra}_{cL}$.

| $\eta$ | $\ell_c$ | $\beta = 1$ | $\beta = 6$ | $\beta = 32$ | $\beta = 50$ |
|---|---|---|---|---|---|
| 0.10 | 1 | 836.55 | 372.57 | 178.72 | 147.08 |
| 0.20 | 2 | 1162.12 | 491.43 | 232.97 | 191.55 |
| 0.25 | 2 | 1283.95 | 544.15 | 257.85 | 212.42 |
| 0.30 | 2 | 1483.25 | 628.39 | 296.49 | 243.92 |
| 0.40 | 3 | 1897.87 | 801.22 | 379.34 | 312.33 |
| 0.50 | 4 | 2491.03 | 1052.10 | 498.15 | 409.96 |
| 0.56 | 5 | 2967.24 | 1254.15 | 594.14 | 488.79 |
| 0.62 | 6 | 3591.17 | 1519.08 | 719.35 | 591.59 |
| 0.65 | 7 | 3984.94 | 1686.66 | 799.02 | 656.92 |

The right hand side in Eq. (A3) is zero. Therefore, taking into account the boundary conditions for the toroidal potential, we get $\tilde{\Psi} = 0$. Hence we have to solve the system of two equations for $\tilde{\Phi}$ and $\Theta$ to derive the critical Rayleigh number. The stability problem has been solved by two methods: the first one by solving a generalized eigenvalue problem [15] and the second one by the time integration of linear Eqs. (12)–(14). Both methods enable the calculation of the leading eigenvalue, $\sigma$, which has the largest real part. Numerical analysis shows that the basic flow becomes unstable with respect to steady perturbations, i.e., $\mathrm{Im}(\sigma) = 0$ for all radius ratios and viscosity contrasts considered. Therefore, as in the case of the Rayleigh-Bénard convection, the first instability does not depend on the Prandtl number. The leading eigenvalue is the growth rate in linear regime, calculated according to $\sigma = \frac{1}{\Delta t}\ln\frac{\Theta(t+\Delta t)}{\Theta(t)}$ because the time dependency of perturbation is proportional to $e^{\sigma t}$. The critical Rayleigh number corresponds to $\sigma = 0$. Results of both methods coincide with accuracy much less than 1%. Furthermore, the critical Rayleigh number at the onset of convection does not depend on the azimuthal wave number $m$. Hence the linear stability equations can be separated for each number $\ell$. Summarizing, the critical Rayleigh number obeys

$$\mathrm{Ra}_{\mathrm{cL}}(\eta,\beta) = \min_{\ell} \mathrm{Ra}_\ell(\eta,\beta). \tag{15}$$

Results of the linear stability analysis are presented in Fig. 1 (note the logarithmic scale for $\mathrm{Ra}_{cL}$) and in Table I. Critical Rayleigh numbers and $\ell_c$ have been calculated as function on radius ratio for $\eta \in [0.1,0.7]$ and for viscosity contrasts $\beta = 1,6,32,50$. A stability analysis for the constant viscosity case ($\beta = 1$) has been performed too and discussed in [3]. Note that critical Rayleigh numbers and $\ell_c$ increase with increasing in $\eta$ for fixed $\beta$. But the temperature-dependent viscosity leads to the remarkable decreasing of the critical Rayleigh numbers $\mathrm{Ra}_{cL}$. Indeed, whereas the onset of convection occurs at $\mathrm{Ra}_{cL} = 836.55$ for $\eta = 0.1$ and at $\mathrm{Ra}_{cL} = 2491$ for $\eta = 0.5$ in the case of the constant viscosity, the critical Rayleigh number shifts to $\mathrm{Ra}_{cL} = 147.08$ for $\eta = 0.1$ and $\mathrm{Ra}_{cL} = 409.96$ for $\eta = 0.5$ for the viscosity contrast $\beta = 50$ (Table I). But, generally, shapes of stability curves for temperature-dependent viscosity ($\beta > 1$) and constant viscosity ($\beta = 1$) are similar. Even intervals, in which the number $\ell_c$ is critical, shift only slightly from one $\beta$ to the other. The next important feature is that the intervals with higher critical numbers $\ell_c$ become very narrow if $\eta$ increases. This provides a multiplicity of the three-dimensional supercritical states.

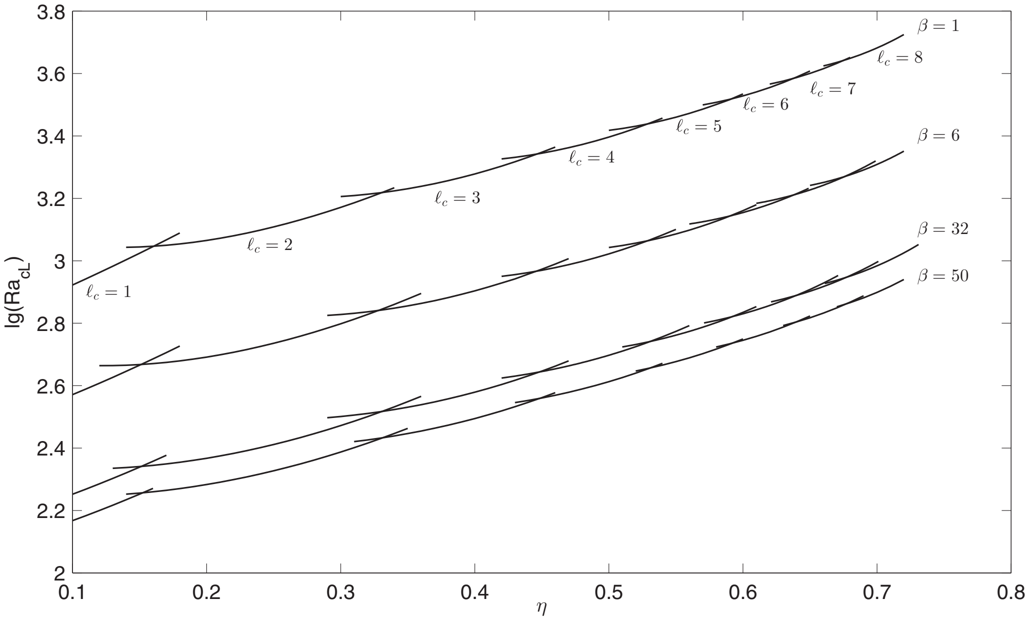

FIG. 1. Critical Rayleigh numbers $\mathrm{Ra}_{cL}$ as function on $\eta$.

## V. 3D DYNAMICS SIMULATION

Solutions of the fully three-dimensional nonlinear problem are necessary for the identification of the three-dimensional structure of the flow. Moreover, results obtained in frames of the linear stability theory can be checked by means of three-dimensional calculations. However, only two bifurcation scenarios are analyzed, since the full analysis of the bifurcation branches would go beyond the scope of this study. The analysis of the three-dimensional flow begins with the presentation of slightly supercritical states. Furthermore, we investigate the behavior of the Nusselt number which is important for the description of the heat transfer. Additionally, experimental results allow one to corroborate numerical simulations. A comparison of numerical and experimental results form the GeoFlow experiment for the case $\eta = 0.5$ and $\beta = 32$ is presented in Sec. VI and ends this study.

### A. Onset of convection

We present the bifurcated branches of solution near the onset of convection using results of local bifurcation analysis with spherical symmetry and time integration. The spherical symmetry of the problem gives information of the kind of bifurcations near the onset of convection [16]. For generic conditions (codimenion-1 bifurcation), the possible bifurcated branches depend only on the $\ell_c$ critical mode [16]. In particular, the bifurcation is (supercritical or subcritical) pitchfork for odd modes and transcritical for even modes. Because of the spherical symmetry, the solution branch belongs to an orbit of solutions obtained by rotation around the centroid. Moreover, note that the pitchfork bifurcation breaks the antipodal symmetry ($\mathbf{r} \to -\mathbf{r}$) noted $S$. However, the solution $X$ and its opposite $S(X)$ belong to the same orbit so, in this paper, we represent only one branch. Moreover, the theory of bifurcation with symmetry allows one to characterize the symmetry of the bifurcated branches at least for $\ell \leqslant 4$ [17]. The definition of symmetry groups relevant for the paper are given in Appendix B. We list the bifurcated branch for $\ell_c \leqslant 4$ as follows.

(i) $\ell_c = 1$. One axisymmetric branch [$\mathrm{O}(2)^-$ symmetry].

(ii) $\ell_c = 2$. One axisymmetric branch [$\mathrm{O}(2) \oplus \mathbb{Z}_2^c$]. This branch crosses the bifurcation point and it is unstable.

(iii) $\ell_c = 3$. Three branches with the symmetries: $\mathrm{O}(2)^-$, $\mathbf{D}_6^d$ (threefold rotations), and $\mathbb{O}^-$ (tetrahedron symmetry). The axisymmetric solution is unstable and there is one stable branch among the $\mathbf{D}_6^d$ and $\mathbb{O}^-$ branches.

(iv) $\ell_c = 4$. Two unstable transcritical branches with the symmetries $\mathrm{O}(2) \oplus \mathbb{Z}_2^c$ and $\mathbb{O}^-$ cross the bifurcation point.

Therefore, the direct time integration is required to determine the stable branch for $\ell_c = 3$, on the one hand, and, on the other, for $\ell_c = 2$ or 4 to find the attractor near the onset since all bifurcated branches are unstable. We present two samples of the slightly supercritical three-dimensional flow for radius ratios $\eta = 0.1$ and $\eta = 0.5$ to examine results given by the linear stability analysis. Dynamic features are characterized by the total kinetic energy of the fluid $E$ that can be represented as summation over the energies $E_\ell$, corresponding to the wave modes $\ell$,

$$E = \frac{1}{2}\int_V \mathbf{u}^2 dV = \sum_\ell E_\ell = \sum_\ell \sum_{m=0}^{\ell} \varepsilon_{\ell m}. \qquad (16)$$

In all cases the conducting state has been used as an initial condition. To produce a three-dimensional flow some spectral coefficients with $m > 0$ [see Eq. (11)] have been perturbed. No symmetry has been assumed. The nonlinear analysis confirms that the basic state [$\mathbf{u}_0 = \mathbf{0}$ and $T_0 = T_{\mathrm{cond}}(r)$] loses stability, if the Rayleigh number exceeds the critical one ($\mathrm{Ra} > \mathrm{Ra}_{cL} = 147.08$) for $\eta = 0.1$ and $\beta = 50$ (Fig. 2). Calculation of energies $E_\ell$ show that the degree $\ell = 1$ is dominant (Table II), which is in good agreement with the linear stability (Table I). Modes $\ell = 1$, $m = 1$ ($\varepsilon_{11} = 0.2968$) and $\ell = 2$, $m = 2$ ($\varepsilon_{22} = 2.1459 \times 10^{-2}$) have a most significant

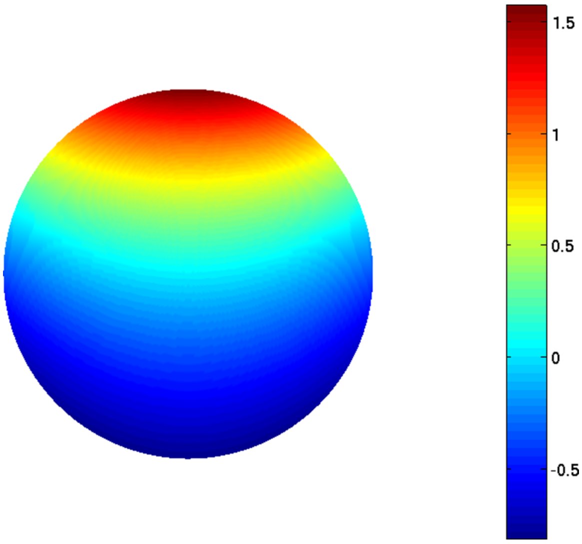

FIG. 2. Radial velocity component for $\eta = 0.1$, Ra = 150, Pr = 125, and $\beta = 50$ in the middle of the gap.

influence on the three-dimensional structure (Fig. 2). Please note that to make the influence of the mode $\ell = 1$, $m = 1$ visible the axisymmetric mode has been eliminated.

In case of radius ratio $\eta = 0.5$ nonlinear calculations, performed with small values of the spectral coefficients that have been used as initial conditions, are in very good agreement with linear stability results, too. The radial component of the three-dimensional steady flow obtained just above $\mathrm{Ra}_{cL}$ has an octahedral (Fig. 3) form as in the case of constant viscosity $\beta = 1$ [5]. But, in case of the temperature-dependent viscosity, e.g., $\beta = 50$, the flow becomes unstable much earlier at $\mathrm{Ra}_{cL} = 409.96$ (Table I). According to the three-dimensional calculations this pattern has two dominant modes (Table III), corresponding to $\ell = 4$, $m = 0$ ($\varepsilon_{40} = 26.6964$) and $\ell = 4$, $m = 4$ ($\varepsilon_{44} = 19.0688$) in qualitative agreement with the analytical result obtained by Busse [4] and Bercovici *et al.* [18].

### B. Bifurcation diagrams

Before we start discussion of the bifurcation diagrams, it is useful to introduce some definitions that are important for the description of the system under consideration. Because the basic flow is absent ($\mathbf{u}_0 = 0$) it is convenient to define the value

$$a = \sqrt{E} \tag{17}$$

as the *amplitude* of the flow. The behavior of the amplitude is controlled by the supercriticality, $\delta = (\mathrm{Ra} - \mathrm{Ra}_{cL})/\mathrm{Ra}_{cL}$, or Rayleigh number *control parameter*.

TABLE II. Kinetic energy of the first four modes for $\eta = 0.1$, Ra = 150, Pr = 125, and $\beta = 50$.

| $\ell$ | $E_\ell$ | $\ell$ | $E_\ell$ |
|---|---|---|---|
| 1 | 0.3151 | 3 | $8.631 \times 10^{-4}$ |
| 2 | 0.0322 | 4 | $3.090 \times 10^{-5}$ |

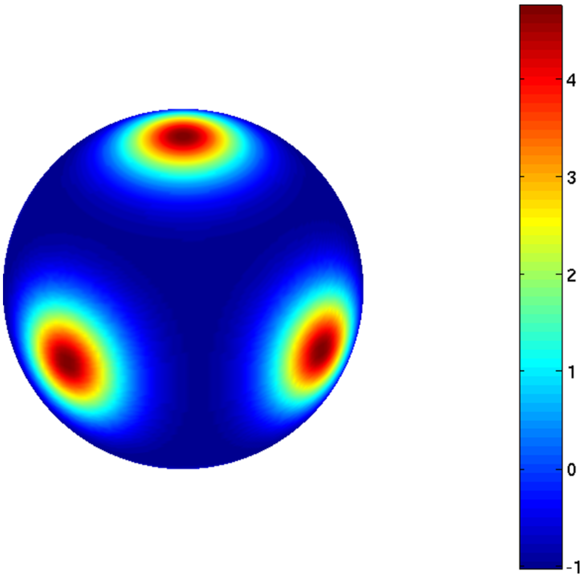

FIG. 3. Radial velocity component for $\eta = 0.5$, Ra = 412, Pr = 125, and $\beta = 50$ in the middle of the gap.

We present only two bifurcation scenarios occurring in gaps with radius ratios $\eta = 0.1$ and $\eta = 0.5$ and for fixed Prandtl number Pr = 125.

Numerical calculations, performed for wide gap ($\eta = 0.1$), show that critical Rayleigh numbers, given by three-dimensional analysis, coincide with $\mathrm{Ra}_{cL}$, obtained by means of the linear stability analysis for all viscosity contrasts considered. The next confirmation of the linear stability results is that the three-dimensional flow is steady. The bifurcation diagram for this situation is presented in Fig. 4. The Navier-Stokes equation has a stable conductive solution at $\delta < 0$. Convection sets in at the bifurcation point $\delta = 0$. If the Rayleigh number exceeds the critical one, $\delta > 0$, the conductive solution loses its stability with respect to infinitesimal perturbations. The instability sets in as a *pitchfork supercritical bifurcation*, because the conductive solution becomes unstable only at $\delta > 0$. Note that the critical degree is $\ell_c = 1$ in agreement with theoretical results. According to the Landau equation [19] the amplitude at the vicinity of the critical Rayleigh number can be approximated by the expression

$$a = C_a(\beta)\sqrt{\delta}. \tag{18}$$

Values of the constant $C_a$ are located between $C_a = 4$ and $C_a = 5$ (Table IV). It it interesting to note that this kind of bifurcation is usual in the case of the constant viscosity, e.g., in the box with free-slip boundaries [20] and in the cylindrical gap [21,22].

TABLE III. Kinetic energy of the most dangerous modes for $\eta = 0.5$, Ra = 412, Pr = 125, and $\beta = 50$.

| $\ell$ | $E_\ell$ | $\ell$ | $E_\ell$ |
|---|---|---|---|
| 4 | 45.7652 | 8 | 2.5291 |
| 6 | 3.0104 | 10 | 0.1732 |

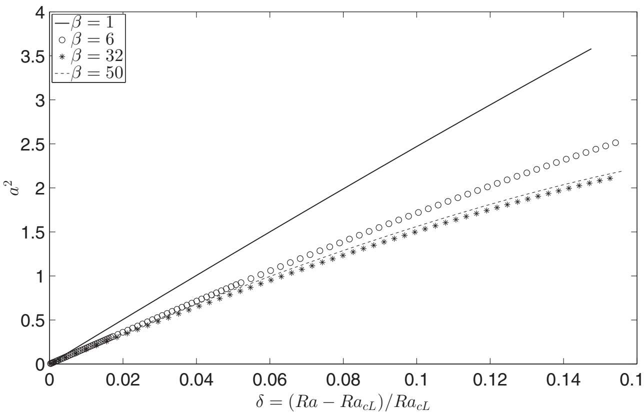

FIG. 4. Amplitude of the supercritical flow for $\eta = 0.1$.

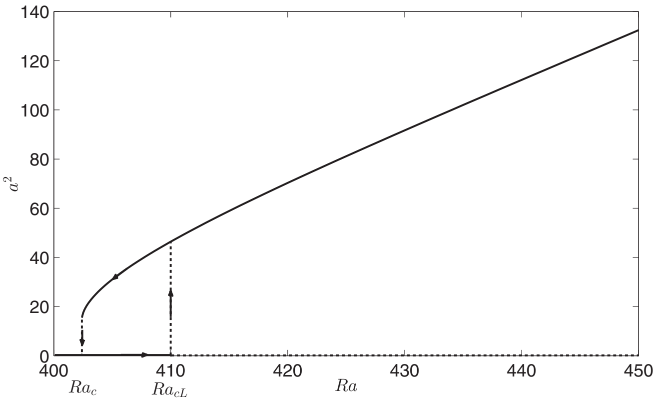

FIG. 5. Amplitude of the flow for $\eta = 0.5$ and $\beta = 50$.

A different bifurcation scenario occurs at $\eta = 0.5$ (Fig. 5). We present the case with $\beta = 50$ in detail. The basic flow loses its stability suddenly at $\mathrm{Ra} = \mathrm{Ra}_{cL} = 409.96$. A branch where $a = 0$ (dotted line in Fig. 5) becomes unstable with respect to infinitesimal perturbations. The transition occurs with a jump into the branch, corresponding to the convective flow (bold line in Fig. 5). The fundamental difference to the above considered case is that the conductive state becomes unstable in the interval $\mathrm{Ra}_G < \mathrm{Ra} < \mathrm{Ra}_{cL}$ ($\mathrm{Ra}_G$ is the Rayleigh number, corresponding to the global stability) if the perturbation is large enough. From the other side, the conductive solution remains stable to infinitesimal perturbations in this region. The transition from the convective branch on the conductive one occurs at $\mathrm{Ra}_c = 402.4$ again with a jump. Hence the *subcritical* instability leads to the hysteresis effect. It suggests that the unstable transcritical branch possesses a turning point in the subcritical region for which the branch gains stability as it is observed in the isoviscous case [5,23]. Note that the same bifurcation scenario takes place for other $\beta$, too. But whereas the difference $\Delta = (\mathrm{Ra}_{cL} - \mathrm{Ra}_c)/\mathrm{Ra}_{cL} = 0.06\%$ is very small in the case of constant viscosity $\beta = 1$ ($\mathrm{Ra}_{cL} = 2491$, $\mathrm{Ra}_c = 2489.4$), the hysteresis effect becomes more remarkable in fluids with high viscosity contrast, e.g., for $\beta = 32$ ($\mathrm{Ra}_{cL} = 498.15$, $\mathrm{Ra}_c = 492.8$) we have numerically found that $\Delta = 1.21\%$ and for $\beta = 50$, $\Delta = 1.84\%$ (Fig. 5).

### C. Behavior of the Nusselt number

The Nusselt number is a global characteristic of the heat transfer that is defined as the ratio between the heat flux of the convective flow and the heat flux of the pure conduction regime, $T_{\mathrm{cond}}(r)$. Expressions for the Nusselt number on the inner and outer surfaces can be formulated as follows:

$$\mathrm{Nu}_{\mathrm{in}} = -\frac{(1-\eta)^2}{4\pi\eta}\int_{S_{\mathrm{in}}}\left(\frac{\partial T}{\partial r}\right)_{\mathrm{in}} dS_{\mathrm{in}}, \tag{19}$$

$$\mathrm{Nu}_{\mathrm{out}} = -\frac{(1-\eta)^2}{4\pi\eta}\int_{S_{\mathrm{out}}}\left(\frac{\partial T}{\partial r}\right)_{\mathrm{out}} dS_{\mathrm{out}}. \tag{20}$$

TABLE IV. Constants $C_a$ and $C_{\mathrm{Nu}}$ for $\eta = 0.1$.

| $\beta$ | $C_a$ | $C_{\mathrm{Nu}}$ |
|---|---|---|
| 1 | 5.02 | 0.4300 |
| 6 | 4.25 | 0.3871 |
| 32 | 4.06 | 0.4037 |
| 50 | 4.19 | 0.4562 |

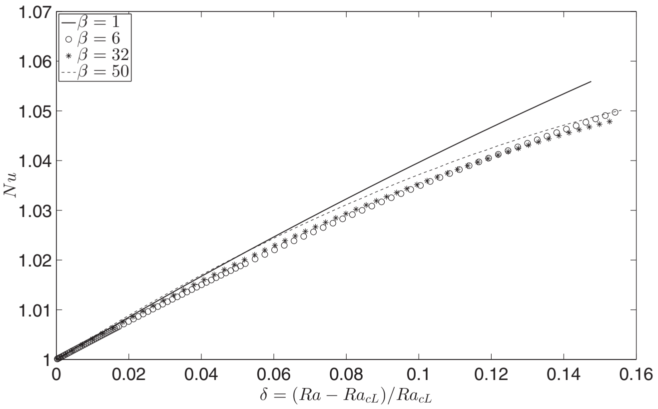

FIG. 6. Behavior of the Nusselt number for $\eta = 0.1$.

Beginning with the case $\eta = 0.1$ (supercritical bifurcation), we note that if the Rayleigh number is smaller than the critical one ($\mathrm{Ra} < \mathrm{Ra}_{cL}$) the Nusselt number is unity and increases if the Rayleigh number exceeds $\mathrm{Ra}_{cL}$ (Fig. 6). It is worth noting that according to the linear stability analysis the threshold of convection does not depend on the Prandtl number. Nevertheless, this dependence appears in the nonlinear case. We concentrate on the influence of the parameter $\beta$ on the flow and heat transfer, because of our interest on the temperature-dependent viscosity in frames of the GeoFlow experiment on the ISS. The behavior of the Nusselt number for slightly supercritical states has a linear shape and changes according to

$$\mathrm{Nu} = 1 + C_{\mathrm{Nu}}(\beta)\delta. \tag{21}$$

Constants $C_{\mathrm{Nu}}(\beta)$ have almost the same value for all $\beta$ considered (Table IV). Moreover, it is worth noting that the influence of the dielectrophoretic effect on the heat transfer in the wide spherical gap is weaker than in the cylindrical one where $\mathrm{Nu} = 1 + 0.92\delta$ for $\eta = 0.1$ [22]. The behavior of the

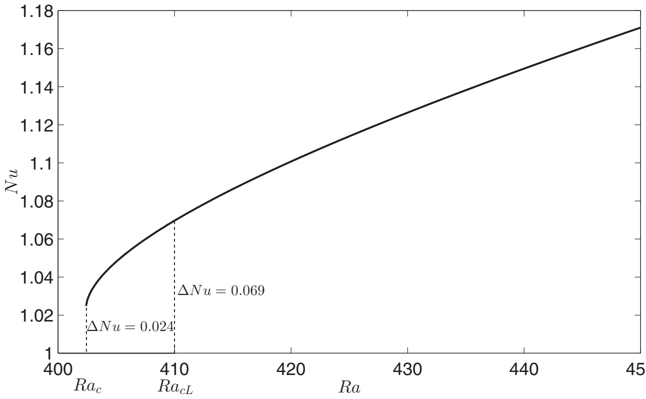

FIG. 7. Behavior of the Nusselt number for $\eta = 0.5$ and $\beta = 50$.

Nusselt number changes drastically for $\eta = 0.5$. A subcritical bifurcation is responsible for the jump of the Nusselt number at Ra = 409.96. Furthermore, the Nusselt number undergoes a remarkable increase in comparison to $\eta = 0.1$ (Fig. 7). Indeed, whereas an increase of the Rayleigh number of 10% for the wide gap leads to a change of the Nusselt number solely in 3%–4%, the same growth of the Rayleigh number for $\eta = 0.5$ causes an enhancement of the Nusselt number of 18% which is interesting from a practical point of view for possible technical applications.

## VI. COMPARISON WITH EXPERIMENT

The GeoFlow experiment [11,24] on the ISS is designed to study convective flows under the influence of a radial force field. The specific experimental setup follows strictly the spherical gap geometry presented in Sec. I. A gap between two concentric spherical shells is filled with a highly viscous dielectric working fluid, namely the straight chain fatty alcohol 1-Nonanol. The radius ratio of $\eta = 0.5$ is in good agreement with geometrical properties of the Earth's outer core and even the Earth's mantle. Convection is triggered by heating the inner shell in steps of $T_{\text{cold}} + \Delta T$, where $(\Delta T)_{\min} = 0.4$ K and the maximum temperature difference is $\Delta T = 10$ K. The experiment is performed at two working environments, $T_{\text{cold}} = 20\,^{\circ}\text{C}$ and $T_{\text{cold}} = 30.5\,^{\circ}\text{C}$, respectively. The lower working environment has a Prandtl number of Pr = 179, whereas the higher temperature level lowers the viscosity and hence the Prandtl number to Pr = 125. The Rayleigh number is changed according to the working environment by a factor of about 20% to higher values. The radial force field is established by utilizing the dielectrophoretic effect, which brings radial accelerations between $0.1\ \text{m/s}^2 < g_e < 13\ \text{m/s}^2$. In consequence of the low acceleration at the outer shell it is necessary to perform the experiment under microgravity conditions. The viscosity contrast of $\beta = 32$ exhibits from the temperature dependent relative permittivity of the working fluid.

The visualization of the fluid flow is a crucial point. However, the safety requirements of the Columbus module make it difficult to work with particles in the fluid. Therefore, a Wollaston sharing interferometry unit is utilized which works by optical means alone. The analysis, interpretation, and postprocessing of these specific interferograms are discussed by various members of the GeoFlow topical team. Depending on the GeoFlow campaign, the interferograms were recorded at different frame rates. In the presented study we use 10 Hz video streams which allow tracking of fluid flows quite accurately. However, this frame rate is more than sufficient for the laminar regime. The recorded period per experimental set point is 2 min, resulting in about 1200 images. In total, 240 parameter variations have been performed during the GeoFlow campaign. The resulting fringe patterns are the base of the following comparisons between numerical simulations and experiments. The experimentally gained Rayleigh numbers are in the range of $10^2 < \text{Ra} < 10^6$, but in the following we focus on experiments for $\text{Ra} < 1.4 \times 10^4$, which are covered by numerical simulations. This regime is dominated by steady laminar flows and conductive states. Due to limitations of the sensitivity in the Wollaston shearing interferometry it is not possible to visualize the onset of convection itself. The lowest technically reachable Rayleigh number is Ra = 560, which is just above the theoretical onset of Ra = 498.15. However, evaluable interferograms are achieved for $\text{Ra} \geqslant 4200$. The high voltage is set to $V_{\text{rms}} = 1800$ V and the reference temperature to $T_{\text{cold}} = 30.5\,^{\circ}\text{C}$. This gives a Prandtl number of Pr = 125, which is used for the numerical simulations, too. Changes in the Rayleigh numbers are only due to temperature variations which are $\Delta T = 1.7$ K. To lower statistical anomalies, we performed all experimental set points twice.

### A. Comparison of numerical and experimental results

In order to validate the theoretical results, we compare numerical interferograms with the experimentally gained images (Fig. 8). The numerical interferograms are calculated by means of the temperature field alone. The radially integrated and weighted temperature field needs to be differentiated directionally in the polarization plane. The resulting temperature fluctuations are visualized by applying a cosine on this field. This gives fringe patterns which are similar to the experimental images [25]. Generic analytical interferograms are subsequently used to distinguish between convective rising plumes and sheetlike flows. The parameter regime of time-dependent convective plumes is above $\text{Ra} = 1.4 \times 10^4$ and not covered by this study. In principle, we observe only threefold and fourfold symmetries of the $m$ mode in the interferograms. These structures exhibit in regular, star-shaped patterns. The detection of $\ell$ mode is not unique, since the optical access does not allow one to investigate the whole lateral elongation. However, we can utilize symmetries in the angles between the sheetlike plumes. The angles between the stripes measure theoretically 120° in the threefold case and 90° in the fourfold case. This geometrical property can be used to identify the $m$ modes. Optical distortions lower and raise the observed angles by 20%–30%, depending on the interferometry direction. The angles between the rays are helpful, but not sufficient for the unique identification. As the experiment rotates very slowly (0.008 Hz, Taylor number $\text{Ta} < 1$), the fringe lines change their relative shape, too. Only by tracking the structures individually is it possible to identify them. Figure 9, first column, presents four experimental set points, namely Ra = 3040, Ra = 4200,

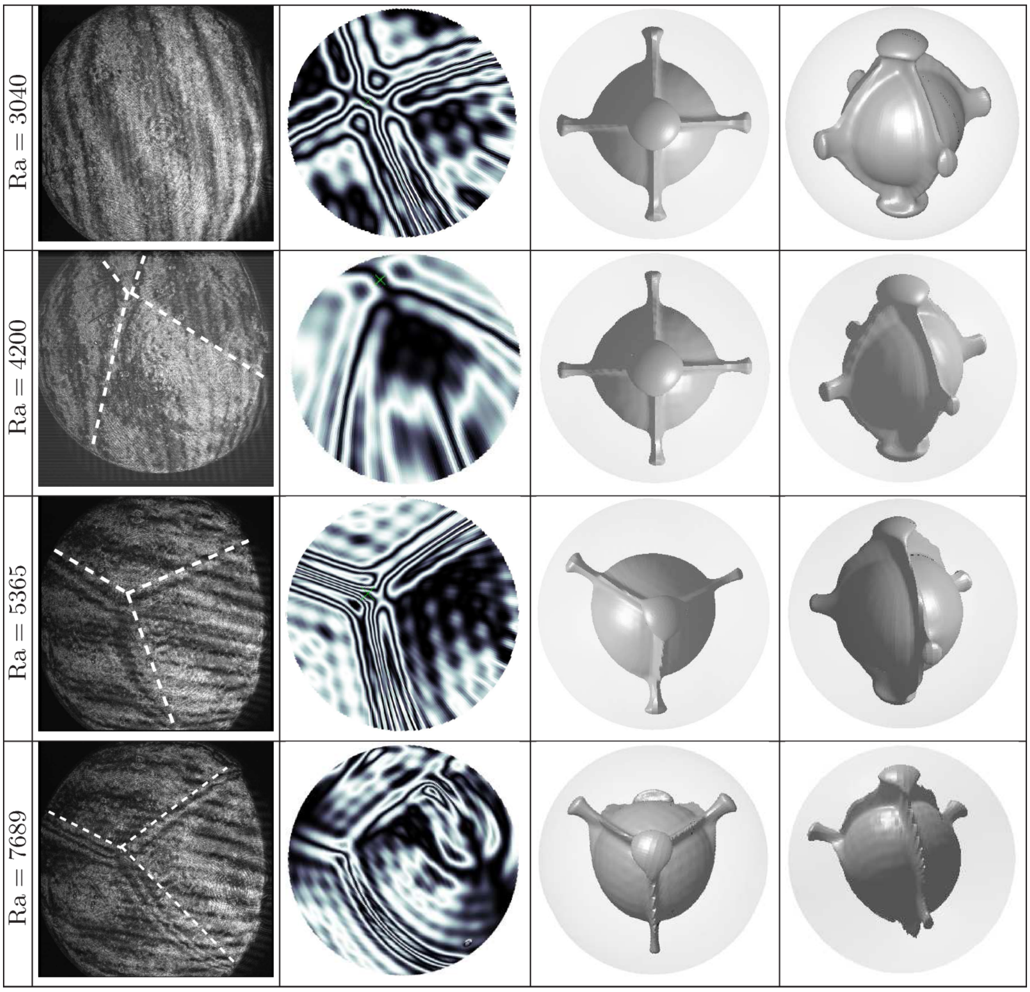

FIG. 8. Comparison of experimental and numerical results for various Rayleigh numbers. From left to right: (1) experimental interferograms from the GeoFlow experiment on the ISS; (2) artificial interferograms calculated by numerical simulations; (3) top view of numerical simulation; (4) side view of numerical simulation. Temperature isosurfaces are calculated at $T = 0.7$. The artificial interferograms show the same modes as the experiments. Even the transition from ($\ell = 4, m = 4$) at Ra = 4200 to ($\ell = 3, m = 3$) at Ra = 5365 is observed. Due to limitations of the interferometry unit, the case of Ra = 3040 shows a false conductive solution.

Ra = 5365, and Ra = 7689. A false (in the sense of interferometry) conductive state is observed: the experimental interferograms do not show significant fringe patterns for Ra = 3040, while according to the stability analysis we expect convective flow. The case Ra = 4200 displays a fourfold mode $m = 4$ which is in good agreement with the numerical analysis that shows that modes ($\ell = 4$, $m = 0$) and ($\ell = 4$, $m = 4$) with energies $\epsilon_{40} = 1458.2$ and $\epsilon_{44} = 5900$ are dominant. As found in the numerical simulations, we identify a transition from $m = 4$ to $m = 3$ as the Rayleigh number is increased from Ra = 4200 to Ra = 5365. Indeed, according to the numerical investigation mode ($\ell = 3, m = 3$) becomes dominant ($\epsilon_{33} = 7354.52$) for Ra = 5365. These patterns are dominant up to Ra = $1.4 \times 10^4$. Higher values exhibit in transient, time-dependent flows. We summarize that the $m = 4$ and the $m = 3$ modes are predominant in the convective laminar regime for $\eta = 0.5$ and $\beta = 32$ in the GeoFlow experiment. In the following, we analyze the symmetry classes in more detail.

### B. Extended analysis of symmetry classes

If the interferometry method allows only identification of the $m$ modes, it is interesting to retrieve the $\ell$-spherical mode of these solutions using DNS. Five cases are analyzed in detail and compared with experimental results. For Ra = 4000 we found two stable states which differ in the $\ell$ mode. The cases of Ra = 3000, Ra = 5365, and Ra = 7000 exhibit in unique states. More specifically, we list the symmetry analysis as follows.

(i) Ra = 3000 and Ra = 4000 ($\ell = 4$). The steady states are a pure $\ell = 4$ mode with the symmetry $\mathbf{D}_4 \oplus \mathbb{Z}_2^c$, i.e., the full group symmetry of a prism with a square basis. This group being a subgroup of the cube symmetry group then, this branch is a secondary branch of the cube symmetric branch (Fig. 5).

(ii) Ra = 4000 ($\ell = 3$). The symmetry group is $\mathbf{D}_6^d$; this threefold symmetric branch bifurcates from the onset of convection of the mode 3. However, according to our numerical results, it is unstable near the onset of convection. Therefore, the stability of the steady state suggests that at least a

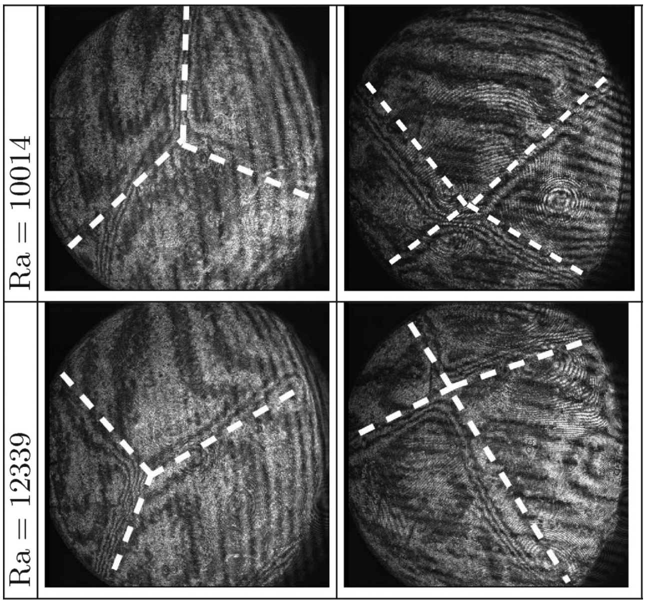

FIG. 9. Hysteresis in the laminar experimental regime: threefold and fourfold symmetries are observed; however, the unstable fourfold symmetry class is more likely in this experiment. In order to lower statistical anomalies, we performed experiments with nonunique patterns several times at different days.

bifurcation occurs and this solution could be a mixed mode (3,4). Therefore, near the bifurcation the mode 4 remains till $\mathrm{Ra} = 4000$. Beyond the mode 3 is in competition with the mode 4.

(iii) $\mathrm{Ra} = 5365$. Almost symmetries of the steady state are broken except a plane reflexion. It is then the $\mathbb{Z}_2^-$ symmetry. It is easy to recognize approximatively the threefold rotation and other plane reflexion, so the symmetry of the solution is close to the $\mathbf{D}_3^z$ or $\mathbf{D}_6^d$ symmetries. The observed mode can be a secondary branch from $\mathbf{D}_6^d$ or $\mathbf{D}_3^z$ branches. All these solutions are possible steady states of the pure mode $\ell = 3$. However, it is possible that the mode 4 coexists. Moreover, note that this $\mathbb{Z}_2^-$ symmetry was not observed near the onset for the (3,4) mode interaction for the isoviscous case (see [15]).

(iv) $\mathrm{Ra} = 7000$. The steady state has the symmetry $\mathbf{D}_2^z$ which corresponds to a twofold reflexion and a plane reflection symmetry. This steady state does not exist for the pure mode $\ell = 3$ but rather for the mode interaction (3,4) (see, e.g., Ref. [15]). Other symmetries are clearly broken, so this steady state is clearly a mixed mode between $\ell = 3$ and $\ell = 4$. The experimental example differs in the Rayleigh number; however, the (3,4) mode is still assumed.

We summarize that the $\ell = 3$ and $\ell = 4$ modes are predominant in the convective laminar regime for $3000 < \mathrm{Ra} < 8000$. By increasing the Ra number, we have the main steps of bifurcation scenario: (a) pure mode 4 steady state; (b) almost "pure" mode 3 steady state; (c) mixed modes 3 and 4.

### C. Hysteresis effect in experiment

The experiments show the existence of multiple stable patterns. This behavior is restricted to a few experiments for $10^4 < \mathrm{Ra} < 1.4 \times 10^4$. At first, the experimental data seemed to be biased by preceding runs. Therefore, we repeated specific set points randomly which reinforced the suspicion that this parameter space exhibits in multiple stable laminar flows. We found the $m = 3$ and the $m = 4$ wave modes at the same Rayleigh number, but in different set points. First results are displayed in Fig. 9. The angles between the rays as well as the (not presented) time lapse are strong evidence that both modes are stable. However, the flow with wave number $m = 4$ mode is less frequent than the flow with $m = 3$. It is assumed that the basin of attraction of the mode $m = 4$ is smaller than for $m = 3$. Similar results are observed in the numerical simulations, where the initial conditions trigger different dominant modes. The randomly initialized flows are an appropriate way to lower these uncertainties.

## VII. CONCLUSION

The presented study deals with the numerical investigation of the convective flow between two spherical surfaces. The inner one is warmer then the outer one. An applied oscillating electrical field produces an artificial radial gravity due to the dielectrophoretic effect. Hence the situation is similar to the Rayleigh-Bénard convection. The influence of the temperature-dependent viscosity has been taken particularly into account. The onset of the convective flow is investigated by means of the linear stability theory that enables one to calculate the critical Rayleigh number, $\mathrm{Ra}_{cL}$, above which the basic flow is always unstable. We found that the temperature-dependent viscosity leads to significant decrease of the critical Rayleigh number. A pseudospectral code developed by Hollerbach [6] and modified for the case of the temperature-dependent viscosity has been used to calculate three-dimensional flows. We present two bifurcation scenarios that occur in spherical gaps with $\eta = 0.1$ and $\eta = 0.5$. Whereas the instability sets in as a supercritical pitchfork bifurcation in the wide gap, if the Rayleigh number exceeds the critical one, the conductive state bifurcates into the convective one with jump, if the gap becomes narrower. The occurring subcritical bifurcation leads to the hysteresis effect. The behavior of the Nusselt number shows that the heat transfer in the wide spherical gap is essentially weaker in comparison to the cylindrical one. Nevertheless the heat transfer grows remarkably if the radius ratio increases. Besides numerical simulations, we compared our results with data from the GeoFlow experiment which is located on the ISS. In order to investigate convection under microgravity conditions, the dielectrophoretic effect is used to maintain an artificial radial force field. The experimental set points reach down to the onset of convection. Evaluable results where found for $\mathrm{Ra} > 4020$, where $m = 4$ and $m = 3$ modes are found. Experimental and numerical interferograms are in good agreement in the presented parameter space. Even regimes with multiple stable structures are observed, where both wave numbers ($m = 3$ and $m = 4$) occur at the same Rayleigh number. Especially the experimental validation confirms the theoretical and numerical results presented in this study.

It is planned to extend the presented study to the rotating case. The GeoFlow experiment has been performed for three rotation rates, 0.008 Hz, 0.8 Hz, and 1.6 Hz. The resulting Taylor numbers $\mathrm{Ta} = (\Omega d^2/\nu)^2$ are below $\mathrm{Ta} = 6 \times 10^4$ for $\mathrm{Ra} < 1.4 \times 10^4$, which can be covered by the presented code.

### ACKNOWLEDGMENTS

The GeoFlow research has been funded by the ESA Grant No. AO-99-049 and by the DLR Grants No. 50 WM 0122 and No. 50 WM 0822. Furthermore, the authors thank the GeoFlow Topical Team (ESA No. 18950/05/NL/VJ), Prof. U. Harlander (Brandenburg University of Technology Cottbus-Senftenberg, Department of Aerodynamics and Fluid Mechanics), and Prof. H. Kuhlmann (TU Wien, Institute of Fluid Mechanics and Heat Transfer) for fruitful discussions. Parallel simulations have been performed at the Northern German Network for High-Performance Computing (HLRN) and the Heraklit cluster at the BTU Cottbus-Senftenberg.

### APPENDIX A: DERIVATION OF EQUATIONS IN THE POLOIDAL-TOROIDAL FORM

In this Appendix we explain how the equations for the poloidal and toroidal potentials in the case of the temperature dependent viscosity can be carried out. Furthermore, we clarify technical details concerning implicit usage of some terms that originally were a part of the friction force. The last term in the Navier-Stokes equation (5) can be written in more useful form. Indeed, introducing the notation $\mathbf{f} = \nabla \cdot [\frac{\nu(T)}{\nu_{\text{cold}}}[\nabla \mathbf{u} + (\nabla \mathbf{u})^T]]$, we have after small algebra

$$\mathbf{f} = \mathbf{f}_0 + \frac{\nu(T_{\text{cond}})}{\nu_{\text{cold}}}\Delta \mathbf{u} + \mathbf{f}_1 + \frac{\nu(T) - \nu(T_{\text{cond}})}{\nu_{\text{cold}}}\Delta \mathbf{u}, \quad \text{(A1)}$$

where

$$\mathbf{f}_0 = \begin{pmatrix} \frac{\nu_r(T_{\text{cond}})}{\nu_{\text{cold}}} D_{rr} \\ \frac{\nu_r(T_{\text{cond}})}{\nu_{\text{cold}}} D_{r\theta} \\ \frac{\nu_r(T_{\text{cond}})}{\nu_{\text{cold}}} D_{r\phi} \end{pmatrix},$$

$$\mathbf{f}_1 = \begin{pmatrix} \frac{\nu_r(\mathrm{T})-\nu_{\mathrm{r}}(\mathrm{T}_{\text{cond}})}{\nu_{\text{cold}}}\mathrm{D}_{\mathrm{rr}} + \frac{1}{\mathrm{r}}\frac{\nu_\theta(\mathrm{T})}{\nu_{\text{cold}}}\mathrm{D}_{\mathrm{r}\theta} + \frac{1}{\mathrm{r}\sin\theta}\frac{\nu_\phi(\mathrm{T})}{\nu_{\text{cold}}}\mathrm{D}_{\mathrm{r}\phi} \\ \frac{\nu_r(\mathrm{T})-\nu_{\mathrm{r}}(\mathrm{T}_{\text{cond}})}{\nu_{\text{cold}}}\mathrm{D}_{\mathrm{r}\theta} + \frac{1}{\mathrm{r}}\frac{\nu_\theta(\mathrm{T})}{\nu_{\text{cold}}}\mathrm{D}_{\theta\theta} + \frac{1}{\mathrm{r}\sin\theta}\frac{\nu_\phi(\mathrm{T})}{\nu_{\text{cold}}}\mathrm{D}_{\theta\phi} \\ \frac{\nu_r(\mathrm{T})-\nu_{\mathrm{r}}(\mathrm{T}_{\text{cond}})}{\nu_{\text{cold}}}\mathrm{D}_{\mathrm{r}\phi} + \frac{1}{\mathrm{r}}\frac{\nu_\theta(\mathrm{T})}{\nu_{\text{cold}}}\mathrm{D}_{\theta\phi} + \frac{1}{\mathrm{r}\sin\theta}\frac{\nu_\phi(\mathrm{T})}{\nu_{\text{cold}}}\mathrm{D}_{\phi\phi} \end{pmatrix},$$

with $T_{\text{cond}} = \frac{\eta}{(1-\eta)^2}\frac{1}{r} - \frac{\eta}{1-\eta}$. This decomposition of the friction term is useful from the numerical point of view because the first two terms in (A1) can be embraced implicitly which increases the numerical convergence. An application of operations $\nabla \times \nabla \times$ and $\nabla \times$ not only eliminates the pressure but also allows one to obtain separated equations for potentials $\Phi$ and $\Psi$,

$$\frac{\Delta_s}{r^2}\left[\frac{1}{\mathrm{Pr}}\frac{\partial}{\partial t}\left(\frac{\partial^2}{\partial r^2} + \frac{\Delta_s}{r^2}\right) - \frac{\nu(T_{\text{cond}})}{\nu_{\text{cold}}}\left(\frac{\partial^2}{\partial r^2} + \frac{\Delta_s}{r^2}\right)^2\right]\Phi$$

$$-\frac{\nu_r(T_{\text{cond}})}{\nu_{\text{cold}}}\Delta_s\left[\frac{2}{r^2}\frac{\partial^3}{\partial r^3} - \frac{2}{r^3}\frac{\partial^2}{\partial r^2} + \frac{2}{r^4}\frac{\partial}{\partial r} + \frac{2}{r^4}\Delta_s\frac{\partial}{\partial r} - \frac{4}{r^5}\Delta_s\right]\Phi$$

$$-\frac{\nu_{rr}(T_{\text{cond}})}{\nu_{\text{cold}}}\Delta_s\left[\frac{1}{r^2}\frac{\partial^2}{\partial r^2} - \frac{2}{r^3}\frac{\partial}{\partial r} - \frac{\Delta_s}{r^4}\right]\Phi$$

$$= \nabla \times \nabla \times \mathbf{F}, \quad \text{(A2)}$$

$$-\frac{\Delta_s}{r^2}\left[\frac{1}{\mathrm{Pr}}\frac{\partial}{\partial t} - \frac{\nu(T_{\text{cond}})}{\nu_{\text{cold}}}\left(\frac{\partial^2}{\partial r^2} + \frac{\Delta_s}{r^2}\right)\right]\Psi$$

$$+\frac{\nu_r(T_{\text{cond}})}{\nu_{\text{cold}}}\Delta_s\left(\frac{1}{r^2}\frac{\partial}{\partial r} - \frac{2}{r^3}\right)\Psi = \nabla \times \mathbf{F}, \quad \text{(A3)}$$

with

$$\Delta_s = \frac{1}{\sin\theta}\frac{\partial}{\partial\theta}\left[\sin\theta\frac{\partial}{\partial\theta}\right] + \frac{1}{\sin^2\theta}\frac{\partial^2}{\partial\phi^2}, \quad \text{(A4)}$$

$$\mathbf{F} = \mathrm{Ra}\frac{\eta^2}{(1-\eta)^4}\frac{T}{r^5}\mathbf{e}_r$$

$$+\mathrm{Pr}^{-1}\mathbf{u} \times (\nabla \times \mathbf{u}) + \mathbf{f}_1$$

$$+\frac{\nu(T) - \nu(T_{\text{cond}})}{\nu_{\text{cold}}}\nabla^2\mathbf{u}. \quad \text{(A5)}$$

There are four boundary conditions for the poloidal potential $\Phi = 0$, $\frac{\partial\Phi}{\partial r} = 0$ and two for the toroidal one $\Psi = 0$ at $r = \frac{\eta}{1-\eta}$ and $r = \frac{1}{1-\eta}$.

### APPENDIX B: SYMMETRY GROUPS

In this section we detail the symmetry groups used in this paper. Let us note $S$ the antipodal symmetry $\mathbf{r} \to -\mathbf{r}$ and $K(\delta)$ the reflection through a plane containing the line $\delta$. Then, we define the following.

(i) The central symmetry group $\mathbb{Z}_2^c$: generated by $S$. Note, it acts trivially on the even modes.

(ii) The symmetry of the cube $\mathbb{O} \oplus \mathbb{Z}_2^c$: generated by the direct symmetries of the octahedron and $S$.

(iii) The symmetry $\mathbb{O}^-$: generated by the direct symmetries of a tetrahedron and by the reflection $K(\delta)$, where $\delta$ is the axis of a threefold rotation of the tetrahedral group.

(iv) Axisymmetric group $\mathrm{O}(2) \oplus \mathbb{Z}_2^c$ (even modes): generated by the rotations about an axis $\delta$ and by $S$.

(v) Axisymmetric group $\mathrm{O}(2)^-$ (odd modes): generated by the rotations about an axis $\delta$ and $K(\delta)$.

(vi) $n$-fold rotation groups (odd modes): $\mathbf{D}_n^z$, generated by the $n$-fold rotation about an axis $\delta$ and $K(\delta)$; $\mathbf{D}_{2n}^d$ contains the $\mathbf{D}_n^z$ group and additionally it possesses a rotation by $\pi$ around an axis perpendicular to $\delta$.

[1] I. Mutabazi, H. N. Yoshikawa, M. T. Fogaing, V. Travnikov, O. Crumeyrolle, B. Futterer, and C. Egbers, Fluid Dyn. Res. **48**, 061413 (2016).

[2] I. Yavorskaya, N. Fomina, and Y. Belyaev, Acta Astronaut. **11**, 179 (1984).

[3] V. Travnikov, C. Egbers, and R. Hollerbach, Adv. Space Res. **32**, 181 (2003).

[4] F. Busse, J. Fluid Mech. **72**, 67 (1975).

[5] F. Feudel, K. Bergemann, L. S. Tuckerman, C. Egbers, B. Futterer, M. Gellert, and R. Hollerbach, Phys. Rev. E **83**, 046304 (2011).

[6] R. Hollerbach, Int. J. Numer. Meth. Fluids **732**, 773 (2000).

[7] B. Futterer, C. Egbers, N. Daley, S. Koch, and L. Jehring, Acta Astronaut. **66**, 193 (2010).

[8] J. Ratcliff, G. Schubert, and A. Zebib, Physica D **97**, 242 (1996).

[9] S. Androvandi, A. Davaille, A. Limare, A. Foucquier, and C. Marais, Phys. Earth Planet. Inter. **188**, 132 (2011).

[10] B. Futterer, N. Daley, S. Koch, N. Scurtu, and C. Egbers, Acta Astronaut. **71**, 11 (2012).

[11] B. Futterer, A. Krebs, A.-C. Plesa, F. Zaussinger, R. Hollerbach, D. Breuer, and C. Egbers, J. Fluid Mech. **735**, 647 (2013).

[12] V. S. Solomatov, Phys. Fluids **7**, 266 (1995).

[13] J. Curbelo and A. M. Mancho, Phys. Rev. E **88**, 043005 (2013).

[14] J. Curbelo and A. M. Mancho, Phys. Fluids **26**, 016602 (2014).

[15] P. Beltrame and P. Chossat, Eur. J. Mech. B: Fluids **50**, 156 (2015).

[16] P. Chossat, R. Lauterbach, and I. Melbourne, Arch. Ration. Mech. Anal. **113**, 313 (1990).

[17] C. Geiger, G. Dangelmayr, J. Rodriguez, and W. Güttinger, in *Pattern Formation: Symmetry Methods and Applications*, Fields Institute Communications, edited by W. L. J. Chadam, M. Golubitsky, and B. Wetton (American Mathematical Society, Providence, RI, 1996), Vol. 5, pp. 225–237.

[18] D. Bercovici, G. Schubert, and G. Glatzmaier, Geophys. Astrophys. Fluid Dyn. **61**, 149 (1991).

[19] L. Landau and E. Lifshitz, *Electrodynamics of Continuos Media*, 2nd ed. (Elsevier Butterworth-Heinemann, Burlington, MA, 1984), Vol. 8.

[20] V. Solomatov and A. Barr, Phys. Earth Planet. Inter. **165**, 1 (2007).

[21] H. Yoshikawa, O. Crumeyrolle, and I. Mutabazi, Phys. Fluids **25**, 024106 (2013).

[22] V. Travnikov, O. Crumeyrolle, and I. Mutabazi, Phys. Fluids **27**, 054103 (2015).

[23] P. Beltrame, V. Travnikov, M. Gellert, and C. Egbers, Nonlin. Process. Geophys. **13**, 413 (2006).

[24] J. M. E. Navarro, J. J. Fernández, J. Rodríguez, A. Laverón-Simavilla, and V. Lapuerta, Microgravity Sci. Technol. **27**, 61 (2015).

[25] F. Zaussinger, A. Krebs, V. Travnikov, and Ch. Egbers, Adv. Space Res. **60**, 1327 (2017).